Available online at www.sciencedirect.com
ScienceDirect

Journal of Computational Physics 220 (2006) 532–548

JOURNAL OF COMPUTATIONAL PHYSICS

www.elsevier.com/locate/jcp

On the multidimensional gas-kinetic BGK scheme

Qibing Li *, Song Fu

Department of Engineering Mechanics, Tsinghua University, Beijing 100084, PR China

Received 8 August 2005; received in revised form 8 July 2006; accepted 17 July 2006
Available online 30 August 2006

Abstract

This paper concerns the performance difference among the multidimensional (MD) gas-kinetic BGK scheme, the corresponding quasi-one-dimensional (Q1D) extension and the directional splitting (DS) scheme with kinetic boundary conditions. The MD scheme includes tangential slopes in the flux calculation, which are absent in a Q1D or DS method. In spite of taking more computational time, the MD scheme is found to be able to capture the characteristics of rarefied flow having a boundary with curvature or a nonuniform temperature, such as the inverted velocity distribution in rarefied cylindrical Couette flow and the weak flow field induced by the temperature gradient of a body, where the Q1D fails. The MD scheme can also yield clearly better results in high-speed microchannel flow and power-law fluid flow between concentric rotating cylinders, when compared with direct simulation Monte Carlo studies and analytic solutions. In the low-Reynolds-number flow around a NACA0012 airfoil case, the MD scheme and the Q1D method predict wall heat flux distribution with obvious difference. The DS method predicts results nearly identical to those from Q1D in these steady flow cases, except that it can hardly give reasonable solutions in power-law fluid case with viscous exponential factor away from unity. Correct prediction of the stress and the wall temperature gradient is considered responsible for this better performance. In simulations of the scalar convection–diffusion equation, it is found that the inclusion of tangential slopes in the flux computation can clearly improve the temporal accuracy of the scheme. In this case, the DS scheme also shows good performance. The present study suggests caution in adopting of the Q1D extension or DS method in multidimensional flow when it is sensitive to the accuracy of stress or wall variable gradient calculations. It is better to use the MD scheme for high-performance simulation.

MSC: 65M06; 76P05; 76N15; 76A05

Keywords: Gas-kinetic scheme; Multidimensional scheme; Quasi-one-dimensional scheme; Directional splitting scheme; Rarefied gas flow; Non-Newtonian fluid flow

---

* Corresponding author. Tel.: +86 10 62788674; fax: +86 10 62772915.
E-mail address: lqb@tsinghua.edu.cn (Q. Li).

0021-9991/$ - see front matter
doi:10.1016/j.jcp.2006.07.010

1. Introduction

Study of a genuinely multidimensional upwind scheme began more than a decade ago with expectations of better characteristics, such as the accuracy [1–3], and efficiency for steady-state flow [4,5], when compared to classical finite-volume methods. Based on the Bhatnagar–Gross–Krook (BGK) gas-kinetic model, an accurate Navier–Stokes flow solver, gas-kinetic BGK scheme, has recently been developed [6–9]. In this scheme, the flux at the cell interface is calculated through the particle distribution function, which is a solution of the Boltzmann–BGK equation with a constructed nonequilibrium initial gas distribution function and an equilibrium state based on cell averaged flow quantities. For efficiency, early versions of the BGK scheme for multidimensional flows are quasi-one-dimensional (Q1D) extensions, or directional splitting (DS) (operator splitting) methods [6,7,10–13]. However, with the inclusion of the tangential slopes of conservative variables in the flux at a cell interface, a truly multidimensional method (MD) can easily be constructed [8,9]. Consideration of all the trajectories with appropriate weighting, according to the number of particles assigned to the trajectory by the BGK solution, endows the scheme with intrinsic upwindedness [14].

In terms of flux evaluation, the MD BGK–NS solver takes 30% more computational time than the Q1D or DS method for two-dimensional flows. However, the differences between the MD and DS BGK schemes in the simulated heat flux and pressure distributions of hypersonic flow are negligible [9]. The large amount of numerical dissipation introduced in the strong shock discontinuity region was considered to be responsible for it, as for the smooth and continuous low speed flows, the MD gas-kinetic scheme [8] was found to give much more accurate results than the corresponding DS method. For three-dimensional flow simulations, the MD scheme is much more expensive and the difference between the MD and Q1D was found to be small for a wide range of problems [15]. Thus the advantage and necessity of adopting the MD scheme still require further study.

In the present work, the performances of the MD BGK–NS solver, the Q1D extension and the DS method are investigated numerically in several typical cases, such as rarefied flow, non-Newtonian fluid flow between rotating cylinders, scalar convection–diffusion flow, and low-Reynolds-number flow around a foil. Before the performance demonstration, the numerical methods are introduced in the next section.

2. Numerical method

In the present study the MD BGK scheme is similar to Xu's method [9], but with a inclusion of a scalar transport [7], through which we expect to evaluate its order of accuracy. Although the treatment of discontinuities is an important characteristic of the BGK method, here it is briefly described in the following by means of a version for smooth flow [8] for simplicity. On the other hand, according to existing studies, as mentioned above, the advantage of using an MD scheme can be better distinguished, without the additional numerical dissipation from flow discontinuities.

2.1. Finite-volume BGK scheme with scalar transport

First, the two-dimensional (2D) BGK–Boltzmann equation can be written as

$$f_t + uf_x + vf_y = (g - f)/\tau, \tag{1}$$

where f is the gas distribution function, g is the equilibrium state approached by f. They are both functions of space x, y, time t, particle velocities (u, v), and internal variable ξ. τ is the particle collision time. The equilibrium state is assumed to be a Maxwellian distribution,

$$g = \rho(\lambda/\pi)^{(K+3)/2} \mathrm{e}^{-\lambda((u-U)^2+(v-V)^2+(\theta-\Theta)^2+\xi^2)}, \tag{2}$$

where $\xi^2 = \xi_1^2 + \xi_2^2 + \cdots + \xi_K^2$, representing the internal energy of particles. $\lambda = 1/(2RT)$ is a function of temperature T. ρ is the gas density. For convenience, capital letters are adopted in this section to represent the macroscopic variables, such as the velocity U, V, and passive scalar Θ and lowercase letters denote microscopic ones. The total number of degrees of freedom K in ξ is equal to $(5 - 3\gamma)/(\gamma - 1) + 1$ for a 2D flow, comprising the independent rotational degrees of freedom and the random motion of particles in the z direction. Here γ is the specific heat ratio of a gas. In particle collisions, f and g satisfy the conservation constraint

$$\int (g-f)\boldsymbol{\psi}\,\mathrm{d}\Xi = \mathbf{0} \tag{3}$$

at any point in space and time, for the conservation of mass, momentum and energy during particle collisions. Here $\mathrm{d}\Xi = \mathrm{d}u\mathrm{d}v\mathrm{d}\theta\mathrm{d}\xi$ is the volume element in phase space with $\mathrm{d}\xi = \mathrm{d}\xi_1\mathrm{d}\xi_2\cdots\mathrm{d}\xi_K$, $\boldsymbol{\psi}$ is the vector of moments

$$\boldsymbol{\psi} = (\psi_1,\psi_2,\psi_3,\psi_4,\psi_5)^{\mathrm{T}} = (1,u,v,(u^2+v^2+\xi^2)/2,\theta)^{\mathrm{T}}. \tag{4}$$

From Eqs. (1) and (3), the finite-volume formulation of the BGK scheme,

$$(\boldsymbol{W}^*)_{ij}^{n+1} = (\boldsymbol{W}^*)_{ij}^{n} + \frac{1}{S_{ij}}\oint_{\partial\Omega_{ij}}\int_{t^n}^{t^n+\Delta t}\boldsymbol{F}^*\,\mathrm{d}t\,\mathrm{d}l \tag{5}$$

can be obtained, where Ω_{ij} is a computational cell with area S_{ij} and boundary $\partial\Omega_{ij}$. The superscript '*' refers to the variable in global coordinates. The flux $\boldsymbol{F}^*$ is calculated, through coordinate rotation, from that in the local coordinates $\boldsymbol{F}$,

$$\boldsymbol{F}^* = (F_1^*,F_2^*,F_3^*,F_4^*,F_5^*)^{\mathrm{T}} = (F_1, n_xF_2 - n_yF_3, n_yF_2 + n_xF_3, F_4, F_5)^{\mathrm{T}}. \tag{6}$$

Here, the local coordinates are constituted with the normal direction $\boldsymbol{n}$ and the tangential direction $\boldsymbol{l}$ of a cell interface. For convenience, the calculation of $\boldsymbol{F}$ is presented through an example at a cell interface $x_{i+1/2,j} = 0$, $-\Delta y/2 \leqslant y_{i+1/2,j} \leqslant \Delta y/2$. The relations between the distribution function f and the macroscopic conservative quantities $\boldsymbol{W}$ and the flux $\boldsymbol{F}$ are given by

$$\boldsymbol{W} = (\rho,\rho U,\rho V,\rho\varepsilon,\rho\Theta)^{\mathrm{T}} = \int f\boldsymbol{\psi}\,\mathrm{d}\Xi, \quad \boldsymbol{F} = \int uf\boldsymbol{\psi}\,\mathrm{d}\Xi. \tag{7}$$

Here the variable $\rho\varepsilon = p/(\gamma-1) + \rho(U^2+V^2)/2$ is the total energy of a gas with pressure p.

Provided that the distribution function at a cell interface is obtained through the reconstruction of the macroscopic variables nearby, the Euler, or Navier–Stokes, or high-order equations, such as the Burnett equations, can be recovered, depending on which order of truncation is adopted in the Chapman–Enskog expansion [16,17]. The fundamental work of a gas-kinetic method is thus to calculate such a distribution function. Numerical fluxes are then computed through Eqs. (7) and (6), and finally the conservative variable at the next time step can be obtained according to Eq. (5).

2.2. Construction of the particle distribution function

The BGK equation (1) has the integral solution

$$f(x,y,t,u,v,\theta,\xi) = \frac{1}{\tau}\int_0^t g(x',y',t',u,v,\theta,\xi)\mathrm{e}^{-(t-t')/\tau}\mathrm{d}t' + \mathrm{e}^{-t/\tau}f_0(x-ut,y-vt,u,v,\theta,\xi), \tag{8}$$

where $x' = x - u(t-t')$, $y' = y - v(t-t')$ is the trajectory of a particle's motion and f_0 is the initial gas distribution function at the beginning of each time step ($t = 0$). Once f_0 and g are obtained, one can easily get the time developing distribution function f. The key of the BGK scheme is thus to construct f_0 and g according to the Chapman–Enskog expansion,

$$f_0(x,y,u,v,\theta,\xi) = g_0[1 - \tau(au+bv+A) + ax + by], \tag{9}$$

$$g(x,y,t,u,v,\theta,\xi) = g_0(1 + ax + by + tA), \tag{10}$$

where terms a, b, A are from the Taylor expansion of a Maxwellian, and a, b are functions of the normal and tangential slopes of conservative variables, and A is the temporal slope. g_0 is the initial Maxwellian at the cell interface,

$$g_0 = \rho_0(\lambda_0/\pi)^{(K+3)/2}\mathrm{e}^{-\lambda((u-U_0)^2+(v-V_0)^2+(\theta-\Theta_0)^2+\xi^2)}. \tag{11}$$

If the flow field is smooth enough, a continuous distribution function across the interface is adopted, the macro conservative variables

$$\boldsymbol{W}_0 = (\rho_0, \rho_0 U_0, \rho_0 V_0, \rho_0 \varepsilon_0, \rho_0 \Theta_0)^{\mathrm{T}} \tag{12}$$

and their gradients at the interface are computed by a linear interpolation. Other high-order reconstruction can also be used to improve the accuracy [8]. The local terms a, b, A have a similar form such as

$$a = a_1 + a_2 u + a_3 v + a_4 (u^2 + v^2 + \xi^2)/2 + a_5 \theta = a_\alpha \psi_\alpha, \quad \alpha = 1\text{–}5. \tag{13}$$

where all coefficients a_α, b_α, A_α are local constants. Then f can be evaluated from f_0 and g through expression (8),

$$f(0,0,t,u,v,\theta,\xi) = g_0[1 - \tau(au + bv + A) + tA]. \tag{14}$$

Thus the fluxes across the cell interface can be calculated with Eq. (7). Then the fluxes in the global coordinates can be obtained through Eq. (6). Finally, the conservative variables at the next time step can be calculated with the finite-volume formulation (5).

The constants a_α, b_α are calculated through their relations with the gradients of macroscopic conservative variables, $\nabla \boldsymbol{W}$,

$$\frac{1}{\rho_0} \nabla_x \boldsymbol{W} = \frac{1}{\rho_0} \int \boldsymbol{\psi} a g_0 \, \mathrm{d}\Xi = \boldsymbol{Ma}, \tag{15}$$

$$\frac{1}{\rho_0} \nabla_y \boldsymbol{W} = \frac{1}{\rho_0} \int \boldsymbol{\psi} b g_0 \, \mathrm{d}\Xi = \boldsymbol{Mb}, \tag{16}$$

where

$$M_{\alpha\beta} = (1/\rho_0) \int \psi_\alpha \psi_\beta g_0 \, \mathrm{d}\Xi, \quad \alpha, \beta = 1\text{–}5. \tag{17}$$

After integration of the above equation, the matrix $\boldsymbol{M}$ can be written with simple components and Eqs. (15) and (16) can be directly resolved to get a_α, b_α, such as

$$a_5 = \frac{2\lambda_0}{\rho_0} \left(\frac{\partial(\rho_0 \Theta_0)}{\partial x} - \Theta_0 \frac{\partial \rho_0}{\partial x} \right), \tag{18}$$

etc. The details can be found in the previous work [7]. Then, from the conservation constraint (3) as well as Eqs. (10) and (14), the relation among a, b and A,

$$\int (au + bv + A) \boldsymbol{\psi} g_0 \, \mathrm{d}\Xi = \boldsymbol{0} \tag{19}$$

can be obtained. Thus A_α can be calculated similarly as

$$\boldsymbol{MA} = -\frac{1}{\rho_0} \int (au + bv) \boldsymbol{\psi} g_0 \, \mathrm{d}\Xi. \tag{20}$$

The collision time τ is given by

$$\tau = \mu_0 / p_0, \tag{21}$$

where μ_0 and p_0 are the macro viscous coefficient and pressure calculated from $\boldsymbol{W}_0$. The time step Δt is calculated from the CFL condition. In the above method, the Prandtl number Pr and Schmidt number Sc are both equal to unity. To simulate a flow with any realistic values of Pr and Sc, a Prandtl number fixing procedure [6] and a special treatment of the calculation of scalar flux [7] can be adopted.

2.3. Kinetic wall boundary condition

Since all the computations in a BGK scheme are based on the particle distribution function, the fluxes at a wall can be easily calculated according to the interaction relation between the gas and a solid boundary

[16,18,19]. The time accurate gas distribution function near the wall f^i can be obtained through the same procedure as that of Eq. (14), with one-side interpolation of the conservative variables initially up to the wall,

$$f^i = g_0[1 - \tau(au + bv + A) + At], \tag{22}$$

in the normal direction, and the wall is assumed to be located at the left cell interface moving with tangential velocity V_w. Thus the number of particles hitting on the wall can be evaluated and these particles will be reflected from the wall with a Maxwell distribution constructed according to the wall temperature λ_w,

$$g^w = \rho_\mathrm{w}(\lambda_\mathrm{w}/\pi)^{(K+3)/2}\mathrm{e}^{-\lambda_\mathrm{w}(u^2+(v-V_\mathrm{w})^2+\theta^2+\xi^2)}. \tag{23}$$

The requirement of no particles penetrating through the solid wall gives,

$$\int_0^{\Delta t}\int_{u<0} uf^i\,\mathrm{d}\Xi\,\mathrm{d}t = -\int_0^{\Delta t}\int_{u>0} ug^w\,\mathrm{d}\Xi\mathrm{d}t, \tag{24}$$

which gives the density near the wall ρ_w,

$$\rho_\mathrm{w} = -\frac{2\sqrt{\pi\lambda_\mathrm{w}}}{\Delta t}\int_0^{\Delta t}\int_{u<0} uf^i\,\mathrm{d}\Xi\,\mathrm{d}t. \tag{25}$$

As the reflected particles may not fully accommodate the wall conditions, the accommodation coefficient, σ, is introduced to represent the diffusive reflection population of particles, and $(1-\sigma)$ for specularly reflected particles. Thus the total gas distribution function at the wall can be written as

$$f^t = \sigma g^w_{u>0} + f^i_{u<0} + (1-\sigma)f^i_{u>0}(-u), \tag{26}$$

where the last term accounts for the component with specular reflection from the wall surface, and '$-u$' means the normal velocity changes its sign and other independent variables remain unchanged.

In high-speed flow, the temperature of the reflected particles may differ from the wall temperature. A thermal accommodation coefficient α can also be introduced similarly to represent the accommodation of the reflected particles with the wall (see [19] for details). Similarly other kinds of solid wall condition can easily be constructed. Through these methods the flux across the solid boundary can be evaluated easily and the velocity slip and temperature jump at wall boundary can be recovered automatically in the BGK scheme.

More than one century ago, based on a similar construction of the distribution function at a wall, Maxwell [20] deduced the well-known velocity slip boundary condition for macroscopic conservative variables, with the assumption of the incident distribution function to be the same as the extrapolation of the asymptotic distribution, after which many progresses have been made in the related fields. More accurate slip boundary condition can be obtained by the analysis of the Knudsen layer, solving a half-space boundary value problem of the linearized kinetic equation, resulting in the Knudsen-layer correction of the distribution function [21]. However, the simple combination of the incident distribution function from the first-order Chapman–Enskog expansion and the reflected distribution function from the diffusive and specular reflection model with engineering accommodation coefficients, leads to the velocity slip and temperature jump which are accurate at least at the first-order of the Knudsen number O(Kn), as a solution of NS equation at low Knudsen number, coming from the first-order Chapman–Enskog expansion, is the solution of Boltzmann equation at the accuracy of O(Kn), wherever outside or inside the thin Knudsen layer.

2.4. Analysis of the multidimensional method

As the particle distribution function in a BGK–NS solver is constructed based on the Chapman–Enskog expansion, as shown in Eqs. (9), (10) and (14), the corresponding approximated control equations for macroscopic conservative variables are the NS equations and the linear convection–diffusion equation. The latter can be simply deduced as follows.

The particle distribution function f in Eq. (14) can be rewritten as

$$f = g - \tau\,\mathrm{D}g, \tag{27}$$

where $\mathrm{D} = \partial_t + u_i\partial_{x_i}, i = 1, 2$. Taking moments of ψ_α again in the BGK equation (1), with the above f, and considering the conservation constraint Eq. (3), we get

$$\int \psi_\alpha \mathrm{D}g\,\mathrm{d}\Xi = \int \tau\psi_\alpha \mathrm{D}(\mathrm{D}g)\,\mathrm{d}\Xi, \quad \alpha = 1\text{–}5, \tag{28}$$

where the variation of collision time τ around a cell interface within a time step is ignored. However, the spatial and temporal variations of τ at different computational cells and different time steps are accounted for by calculating τ cell by cell based on the local viscosity and pressure (see Eq. (21)). Similar treatment is adopted to get the analytic solution of BGK equation (8). One can see the left side of above equation,

$$L_\alpha \equiv \int \psi_\alpha \mathrm{D}g\,\mathrm{d}\Xi = \mathrm{O}(\tau), \quad \alpha = 1\text{–}5. \tag{29}$$

For $\psi_5 = \theta$, it becomes

$$L_5 \equiv \int \theta\mathrm{D}g\,\mathrm{d}\Xi = \int \theta(g_{,t} + u_l g_{,l})\,\mathrm{d}\Xi = \langle\theta\rangle_{,t} + \langle\theta u_l\rangle_{,l} = \mathrm{O}(\tau), \tag{30}$$

where $\langle(\cdots)\rangle \equiv \int(\cdots)g\,\mathrm{d}\Xi$ is used to simplify the notation. Similarly, the right side of Eq. (28) for $\psi_5 = \theta$ is,

$$R_5 \equiv \int \tau\theta\mathrm{D}(\mathrm{D}g)\,\mathrm{d}\Xi = \int \tau\theta(g_{,tt} + 2u_k g_{,tk} + u_l u_k g_{,lk})\,\mathrm{d}\Xi = \tau[\langle\theta\rangle_{,tt} + 2\langle\theta u_k\rangle_{,tk} + \langle\theta u_k u_l\rangle_{,lk}]. \tag{31}$$

To eliminate the terms contain time derivatives in the above equation, we can consider

$$L_{5,t} = \langle\theta\rangle_{,tt} + \langle\theta u_k\rangle_{,tk} = \mathrm{O}(\tau) \tag{32}$$

and the continuity equation

$$L_1 = \langle 1\rangle_{,t} + \langle u_k\rangle_{,k} = \rho_{,t} + (\rho U_k)_{,k} = \mathrm{O}(\tau). \tag{33}$$

Then Eq. (31) can be simplified as,

$$\begin{aligned} R_5 &= \tau[\langle\theta u_k\rangle_{,t} + \langle\theta u_k u_l\rangle_{,l}]_{,k} + \mathrm{O}(\tau^2) = \tau[(\Theta\rho U_k)_{,t} + (\Theta U_k U_l)_{,l}]_{,k} + \mathrm{O}(\tau^2) = \tau\{\Theta[(\rho U_k)_{,t} \\ &\quad + (\rho U_k U_l + p\delta_{kl})_{,l}] + U_k[(\rho\Theta)_{,t} + (\rho\Theta U_l)_{,l} - \Theta\rho_{,t} + \Theta(\rho U_l)_{,l}] + p\Theta_{,k}\}_{,k} + \mathrm{O}(\tau^2) \\ &= \tau[\Theta L_k + U_k(L_5 - \Theta L_1) + p\Theta_{,k}]_{,k} + \mathrm{O}(\tau^2) = \tau(p\Theta_{,k})_{,k} + \mathrm{O}(\tau^2) = (D\Theta_{,k})_{,k} + \mathrm{O}(\tau^2), \quad k, l = 1, 2. \end{aligned} \tag{34}$$

Here the diffusion coefficient $D = \tau p$ is equal to the viscosity coefficient. That is, the Schmidt number is equal to unity. Finally, combining Eqs. (28), (30) and (34) and dropping terms of $\mathrm{O}(\tau^2)$, one can obtain the linear convection–diffusion equation, as shown along with the NS equations in the following,

$$\frac{\partial \boldsymbol{W}}{\partial t} + \frac{\partial(\boldsymbol{F}_1^{iv} - \boldsymbol{F}_1^{vis})}{\partial x} + \frac{\partial(\boldsymbol{F}_2^{iv} - \boldsymbol{F}_2^{vis})}{\partial y} = \boldsymbol{0}, \tag{35}$$

where

$$\begin{aligned} &\boldsymbol{F}_1^{iv} = (\rho U, \rho U^2 + p, \rho UV, (\rho\varepsilon + p)U, \rho\Theta U)^{\mathrm{T}}, \\ &\boldsymbol{F}_2^{iv} = (\rho V, \rho UV, \rho V^2 + p, (\rho\varepsilon + p)V, \rho\Theta V)^{\mathrm{T}}, \\ &\boldsymbol{F}_i^{vis} = (0, \sigma_{1i}, \sigma_{2i}, s_{3i}, s_{4i})^{\mathrm{T}}, \\ &\sigma_{ij} = \tau p(U_{i,j} + U_{j,i}) + (\varsigma - 2\tau p/3)U_{k,k}, \\ &s_{3i} = U_k\sigma_{ki} + 0.25(K + 4)\mu(1/\lambda)_{,i}, \\ &s_{4i} = \tau p\Theta_{,i}, \quad i, j = 1, 2. \end{aligned} \tag{36}$$

The bulk viscosity from the BGK model is $\varsigma = 4\tau p/15$ for a diatomic gas.

In an MD scheme, the flux across a cell interface in the local rotated coordinates is aligned with both the normal and tangential slopes of the conservative variables. For a Q1D extension, only the normal slopes are considered and the tangential slopes are omitted. It is the same for a DS scheme, although the latter contains a multistep procedure: first to calculate the flow-field $\boldsymbol{W}^{n+1/2}$ at time $t^{n+1/2}$ through the flux along the i direction, and then compute the flux along the j direction based on $\boldsymbol{W}^{n+1/2}$ to get the conservative variables $\boldsymbol{W}^{n+1}$ at time t^{n+1}. In the present study, Godunov splitting [10] is considered. According to Eq. (35), the tangential slopes seem to contribute to only the viscous stress σ, and thus affect the numerical viscous flux (In the next section, we shall find that they may affect the temporal accuracy of the scheme in the unsteady scalar convection–diffusion). For example, consider the flux (stress) across a cell interface in the x direction,

$$\begin{aligned}\sigma_{11} &= 2\mu\partial_x U + (\varsigma - 2\mu/3)(\partial_x U + \partial_y V),\\ \sigma_{12} &= \mu(\partial_x V + \partial_y U).\end{aligned} \tag{37}$$

For a Q1D or DS method, the tangential slopes are omitted, with $b_\alpha = 0$, $\alpha = 1$–5 in the MD scheme. Thus the stress becomes

$$\begin{aligned}\sigma_{11}^N &= 2\mu\partial_x U + (\varsigma - 2\mu/3)\partial_x U,\\ \sigma_{12}^N &= \mu\partial_x V.\end{aligned} \tag{38}$$

Compared to Eq. (37), the above stress in the Q1D expansion and the DS method cannot recover the strain rate tensor and the corresponding viscosity depends on the local rotation. It is true for any type of mesh, not only unstructured, but also Cartesian mesh [22]. One can imagine that this omission of tangential derivatives may result in an evident error in viscous flow simulations, especially for low-Reynolds-number flows. Another situation is, if a flow is dominated by the tangential slopes of variables at a wall, such as thermal creep flow controlled by wall temperature gradient, although the effect of tangential slope can be taken into account in the flux across the cell interface normal to the wall, the omission of it may decrease the accuracy of a simulation. However, for inviscid or high-Reynolds-number flow, a quasi-one-dimensional formulation or directional splitting version may be a good choice, as a multidimensional gas-kinetic reconstruction is much more expensive, with about one third additional CPU time to calculate the flux related to tangential derivatives for two-dimensional flows. For three-dimensional flows, this additional cost is more considerable, with about a 50% increase. In the following, several tests are presented to investigate the necessity to use the MD BGK scheme.

3. Numerical experiments

Six cases are tested with the MD and Q1D gas-kinetic BGK schemes, respectively, such as rarefied cylindrical Couette flow, thermal creep flow, high-speed microchannel flow, power-law fluid flow between rotating cylinders, scalar convection–diffusion, and flow around a NACA0012 airfoil. The first four flows are dominated by viscosity, thus the above-mentioned solvers for smooth flow are adopted, and the advantage of using an MD scheme is expected to be better distinguished. For the last two cases, the general BGK method, with a discontinuous particle distribution function, is used to investigate general multidimensional effects. To accelerate the convergence of the flow to steady state except for the scalar convection–diffusion case, the lower–upper symmetric Gauss–Seidel (LU-SGS) implicit technology [23] is adopted. A steady solution is obtained when the residual error for density is less than 1×10^{-6}. The criterion is 1.5×10^{-8} for momentum in the non-Newtonian flow case. The DS method is also considered in all the above-mentioned cases, only in the explicit version which is expensive in steady flow simulation. It is found that the DS method predicts results nearly identical to those from the Q1D scheme for steady flows, except for the power-law fluid flow case with viscous exponential factor away from unity, in which a reasonable flow-field can hardly be obtained. Thus the DS results in these cases are not presented for the conciseness. All the results show good mesh convergence. Except for special explanations, they are not presented here because of the length limit of the article.

3.1. Cylindrical Couette flow

At first a rarefied cylindrical Couette flow is considered with a rotating inner cylinder of $R_1 = 3\lambda$, a stationary outer cylinder of $R_2 = 5\lambda$, and argon between them with mean free path $\lambda = 6.25 \times 10^{-8}$ m at initially stationary STP conditions ($p_0 = 1.0133 \times 10^5$ Pa, $T_0 = 273.15$ K). Recent analytical and molecular dynamics studies [24–28] suggest that the velocity profile in this case can become inverted for a small accommodation coefficient, where the annular velocity of the gas becomes greater farther away from the moving center.

The MD and Q1D gas-kinetic BGK schemes are applied to this flow with the angular velocity of the inner cylinder $\omega = 5.17 \times 10^8$ rad/s. Thus the tangential velocity of the inner cylinder is about a third of sound speed. The wall temperature is $T_w = T_0$ and the accommodation coefficient σ is 0.1. The computational mesh is uniform in the circumferential direction, with cell number 100, and nonuniform in the radial direction, with cell number 40 and minimal cell size 1.3×10^{-9} m near the solid walls.

Fig. 1 shows the predicted circumferential velocity profiles compared with the direct simulation Monte Carlo (DSMC) results [24] and the analytical solution from the Navier–Stokes equations with Maxwell's general slip condition [29]. The result from the MD gas-kinetic BGK scheme shows good agreement with the analytical solution. Both have inverted annular velocity along the radial direction. That is, the gas travels faster near the stationary outer wall. This distribution has been confirmed by other approximations [25,27]. The deviation from DSMC data may come from the high rarefaction degree of the flow for which a high-order model such as the Burnett equation is more suitable than the Navier–Stokes model.

On the contrary, the Q1D BGK scheme is not able to capture this important aspect of the physics of the velocity inversion process. The calculated normalized annular velocity decreases along the radial direction and is nearly identical to the analytical result from Maxwell's conventional slip condition [29]. The difference between Maxwell's general slip condition and the conventional one is that the former accounts correctly for shear stress at the solid wall by considering both the tangential slope of the normal velocity and the normal slope of the tangential velocity. For a wall with curvature, or with rotational motion, such as a deflecting flap, these two slopes can be of the same magnitude and cannot be neglected.

For the MD gas-kinetic BGK scheme, one can similarly understand the importance of the inclusion of the tangential slopes (terms related to b in the last section) in the fluxes at a cell interface.

3.2. Thermal creep flow

Thermal creep flow, induced by the nonuniform temperature of a body, has been known for a long time [21,30,31]. Here the flow between two stationary parallel plane walls (at $y = 0$ and $y = L$) with the same temperature distribution

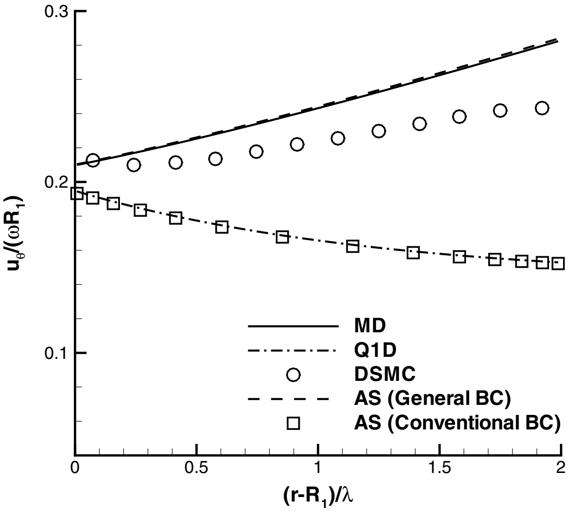

Fig. 1. Nondimensional velocity profiles in cylindrical Couette flow. The symbol 'MD' represents the result with the multidimensional gas-kinetic BGK scheme and 'Q1D' the quasi-one-dimensional extension. The DSMC data is from Ref. [24] and the analytical solution, labeled as 'AS', is from the study of Barber et al. [29] with Maxwell's general and conventional slip conditions.

$$T_w = T_0[1 - \Delta\tau_w \cos(2\pi x/L)] \tag{39}$$

is considered, where L is the distance of the two walls and T_0, $\Delta\tau_w$ are constants. For a slightly rarefied gas, the induced flow velocity is shown with the same order as the Knudson number [21], which cannot be easily captured by a numerical method.

In the present study the Knudson number $Kn = \lambda/L = 0.005$, pressure $p_0 = 1.0133 \times 10^5$ Pa, temperature $T_0 = 273.15$ K with constants $\Delta\tau_w = 0.5$ are adopted. Here the mean free path is calculated with $\lambda = 3.2(2\pi RT_0)^{-1/2}\mu_0/\rho_0$ and $\rho_0 = p_0/(RT_0)$. The computation is started with an initial flow field with zero velocity and constant pressure p_0 throughout. The initial temperature is set same as that of the wall (Eq. (39)) along the x-direction and uniform along the y-direction. After steady flow is established, the pressure in the field shows some increase to about 1.18×10^5 Pa. The gas is supposed to be nitrogen with a viscosity given by Sutherland's law, $\mu = \mu_{\mathrm{ref}}(T/T_{\mathrm{ref}})^{1.5}(T_{\mathrm{ref}} + T_s)/(T + T_s)$, $\mu_{\mathrm{ref}} = 1.663 \times 10^{-5}$ Pa s, $T_{\mathrm{ref}} = 273.15$ K, $T_s = 106.7$ K, the specific heat ratio, $\gamma = 1.4$, and the Prandtl number, $Pr = 0.718$. In view of symmetry, the computational domain is chosen as $0 \leqslant x \leqslant L/2$ and $0 \leqslant y \leqslant L/2$, similar to the study of Sone [31]. 40×40 computational cells are used and the cell size is uniform in the x-direction and stretched in the y-direction with the minimal cell size (at the wall) $\Delta y_{\min} = 0.2\Delta x$.

Fig. 2 shows the temperature fields calculated with the MD BGK and Q1D scheme. Generally, both results are consistent with those from the asymptotic theory [31]. But the difference of the results between MD and Q1D scheme is obvious. More importantly, it should be noted that the induced velocity in Fig. 2 is computed with the MD scheme, and the velocity from the Q1D scheme with the same computational mesh is about two or three magnitudes less. This can be observed in Fig. 3 where the velocity captured by the Q1D scheme is nearly zero. Similar results are obtained with the DS method, although they are somewhat better than the Q1D prediction. The maximal normalized velocity near the wall predicted by MD is achieved at about $x/L = 0.29$ with value 0.0036, in good agreement with the asymptotic solutions of kinetic theory (about 0.0041). It should be noted that the actual Knudsen number computed according to the averaged density of final steady state is about 0.0044, less than that for the asymptotic theory, 0.005. However, the difference between the present MD results and the asymptotic solution, may also come from the different viscosity model and other rarefied effects not being taken into account, such as the nonlinear thermal stress and other high-order effects. Different wall boundary conditions, obtained by the analysis of the Knudsen layer in the asymptotic solution and simply constructed through the Chapman–Enskog expansion in the present study, including the wall temperature jump, not being considered in the former, may also take some responsibility for the disagreement.

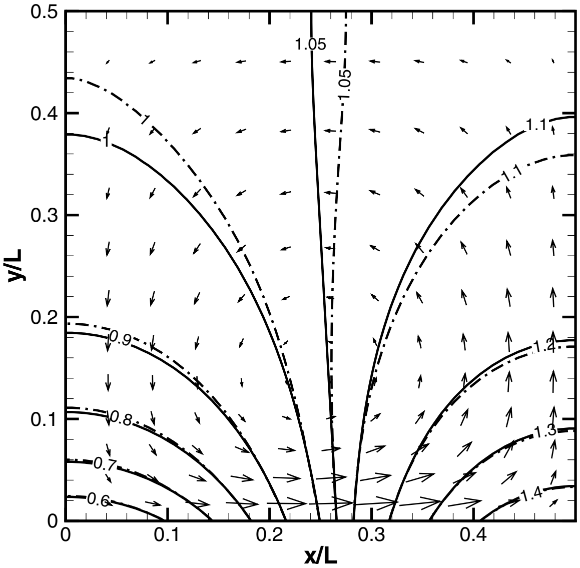

Fig. 2. Temperature and velocity fields between two stationary parallel plane walls. Dash-dot contours are from the Q1D BGK scheme, and solid contours and velocity vectors from the MD scheme. The vector length is proportional to the velocity magnitude.

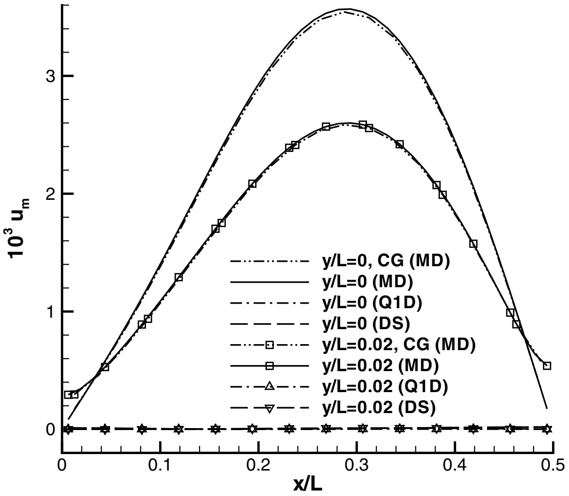

Fig. 3. Flow velocity distribution at $y = 0$ and $y = 0.02$, calculated with the MD, Q1D and DS BGK schemes. The normalized velocity is $u_m = (u^2 + v^2)^{1/2}/\sqrt{2RT_0}$. The symbol 'CG' refers to the solution with 20×20 computational cells.

As the induced flow is very weak in this case, the computation should be carried out very carefully. As shown in Fig. 3, good mesh convergence is obtained, confirming the accuracy of the present results.

Interestingly, we observe that, when the flow is computed with the Q1D scheme and multidimensional kinetic boundary conditions, that is, $b_\alpha = 0$, $\alpha = 1$–5 is not set only in Eq. (22), a satisfactory result can also be obtained, except the maximal velocity is somewhat less than the MD result. This is understandable since the flow is weak and dominated by the wall temperature gradient, thus the inclusion of tangential slopes in the flux only at the wall can significantly improve the result. For cylindrical Couette flow and high-speed microchannel flow (in the following), only multidimensional boundary conditions, or with multidimensional scheme only near the wall (within one or two cells), it is found not easy to obtain a convergent solution. This may come from the inconsistency of the fluxes from MD and Q1D across different interfaces of a cell at the boundary.

In brief, the MD BGK scheme can correctly resolve the weak flow field induced by nonuniform temperature of a wall, whereas the corresponding Q1D and DS schemes fail. Without inclusion of the tangential slopes of conservative variables, the Q1D and DS cannot accurately account for the effects of wall temperature gradient in the flux computation, and thus cannot capture the induced flow field.

3.3. High-speed microchannel flow

The characteristics of the flow in microchannels are important for micro-electro-mechanical systems (MEMS), such as microheaters, microheat exchangers/sinks for electronic cooling and microspacecraft controls. Rarefaction, compressibility and thermal creep dominate the flow in most of the MEMS, as well as the surface forces, roughness and viscous forces. Previous studies show that the gas-kinetic BGK scheme is able to capture these dominating effects at small Knudsen numbers, such as $Kn < 0.4$ [7,16,18]. Here the Knudsen number is defined with channel height H, $Kn = 16\mu/(5\rho H\sqrt{2\pi RT})$.

In the present study, the performance of the MD BGK scheme and the Q1D method are investigated in microchannel flow with high-speed inflow. The computational parameters are chosen to be the same as in case 2 of Oh et al. [32] with channel length $L = 5$ µm, height $H = 1.2$ µm and wall temperature $T_w = 298$ K. The pressure is set to 1.01×10^5 Pa at both the inlet and outlet. The inflow is supersonic helium, $Ma = 5.0$, with temperature $T = T_w$, specific ratio $\gamma = 5/3$, Prandtl number $Pr = 0.704$ and $R = 2076.9$ J/kg K. The viscosity is given by $\mu = \mu_0(T/T_0)^\omega$ with $\mu_0 = 1.865 \times 10^{-5}$ N s/m^2, $T_0 = 273.15$ K, and $\omega = 0.67$. For symmetry about the centerline of the microchannel, only half domain is computed to reduce the CPU time, with 296×40 cells and the minimal cell size $\Delta x = 0.009$ µm at the inlet and outlet and $\Delta y = 0.006$ µm at the wall. Similar to case 1 of Raju and Roy [33], two additional freestream regions are specified with length 1 µm near the inlet and

0.2 μm near the outlet where the accommodation coefficient $\sigma = 0$ is adopted at the wall, and otherwise it is set to be $\sigma = 1$.

Fig. 4 shows the temperature and velocity distributions near the microchannel wall. In general, the present results with gas-kinetic BGK scheme agree well with the DSMC data [32] and can be observed better than the result of Raju and Roy [33] with a finite element based hydrodynamic model and first-order slip boundary conditions. Furthermore, the MD scheme yields better results, with larger temperature jump and velocity slip, than the Q1D scheme, when compared with the DSMC data. The flow-induced temperature modification at the wall is correctly taken into account by the inclusion of tangential slopes in fluxes in the MD scheme. Thus better results can be obtained. This improvement of the wall quantities distribution by an MD scheme can also clearly lead to better results throughout the flow-field (shown in Fig. 5), when compared with the DSMC results [32], although both can capture the flow structures, such as the detached bow shock waves in front of the leading edge, formed because of the viscous boundary layer. The intersection of the leading shocks and reflections from the wall, which usually exist in macro channel flow, cannot be clearly seen due to the strong viscous diffuse.

3.4. Non-Newtonian fluid flow between concentric rotating cylinders

For macro flow the multidimensional scheme is also expected to yield better results than Q1D. Here the cylindrical Couette flow with a power-law fluid is considered. The dimensionless radius of the inner and outer cylinders are $R_1 = 1.0$ and $R_2 = 2R_1$ along with 100 cells in the circumferential direction and 50 in the radial. The inner cylinder is rotating with angular velocity $\omega = 1.0$ and the outer is stationary. The apparent viscosity of the fluid is given by the power-law,

$$\mu = \mu_0 S^{n-1}, \tag{40}$$

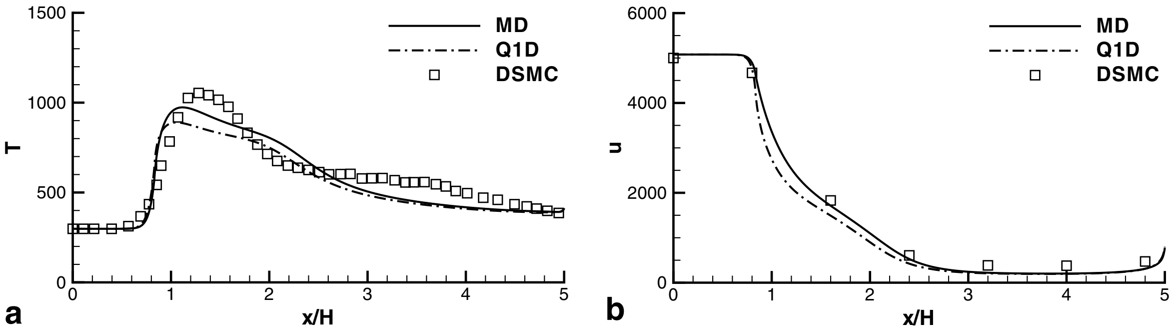

Fig. 4. Wall ($y = 0$) profiles: (a) temperature and (b) streamwise velocity. The DSMC data are from Ref. [32].

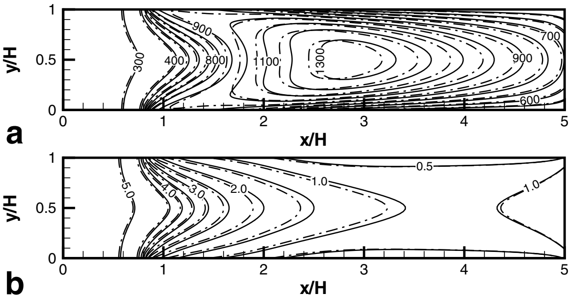

Fig. 5. Contours at steady state: (a) temperature and (b) Mach number. Solid line represents the result with the MD scheme and dash line the Q1D scheme.

where S is strain rate of the flow, $n > 0$ is the exponential factor, and $\mu_0 = 0.02$. Factor $n = 1$ corresponds to a Newtonian fluid, $n > 1$ shear-thinning fluid and $n < 1$ means shear thickening. The initial density is given as $\rho = 1.0$, pressure $p = 1/(\gamma M^2)$ with $\gamma = 1.4$ and Mach number $M = 0.01$ to approach incompressible flow. Nonslip isothermal wall boundary conditions [6] are adopted. The gradients of velocities in the strain rate are from the reconstruction of macroscopic variables at a cell interface for each computational time step. For an incompressible flow, the analytic solution can be deduced as,

$$u_\theta(r) = \frac{\omega}{R_1^{-2/n} - R_2^{-2/n}}(r^{-2/n} - R_2^{-2/n})r. \tag{41}$$

It can be seen in the above expression that when $n < 2$ the circumferential velocity profile is concave, for $n = 2$, linear, and for $n > 2$, convex.

In the present study, four cases are calculated with exponential factors $n = 1.4$, 1, 0.6 and 0.2, respectively. For $n = 1$ the MD and Q1D schemes produce identical results and both agree with the analytic profile excellently, as shown in Fig. 6. With decreasing n the result from the MD scheme can be observed to still be in good agreement with the analytic solution, but the result from the Q1D method shows larger and larger deviation, such as for the case with $n = 0.2$. In the case with the factor away from unity, the DS scheme is found not be able to give convergent flow field, or solution close to that from MD and Q1D, which is different from other steady flow cases in the present study. For a power-law fluid, the apparent viscosity is strongly affected by the strain rate when the exponential factor is far away from unity. Thus the results are sensitive to the accuracy of the shear stress computation. The Q1D/DS scheme is not able to give an accurate stress at a cell interface, resulting in great errors in the corresponding calculated velocity. Similar situations should be paid attention to, such as in turbulence modeling, where the vortex viscosity is also a function of the strain rate of the averaged velocity.

3.5. Square wave convection and diffusion

It is difficult to evaluate accurately a multidimensional solver for compressible flow, for the lack of an analytic solution. To further study multidimensional effects, the accuracies of both MD and Q1D schemes are verified by simulation of the scalar transport equation

$$\Theta_t + U\Theta_x + V\Theta_y = D(\Theta_{xx} + \Theta_{yy}) \tag{42}$$

with initial condition

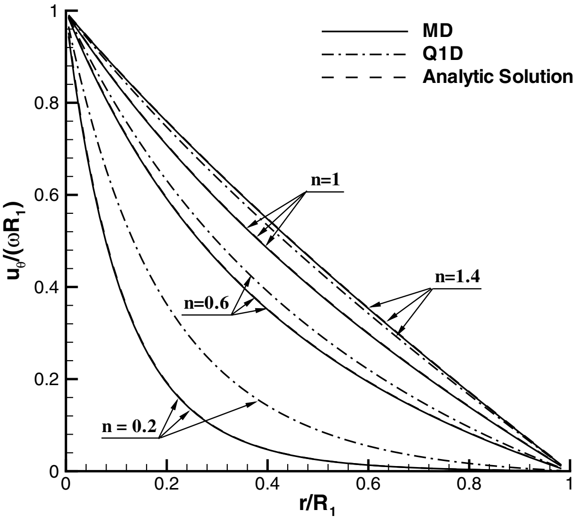

Fig. 6. Nondimensional velocity profiles in cylindrical Couette flow with power-law fluid.

$$\Theta = \begin{cases} 1 & \text{if } \alpha \leqslant x \leqslant \beta \quad \text{and} \quad \alpha \leqslant y \leqslant \beta, \\ 0 & \text{else}, \end{cases} \tag{43}$$

where α, β are constants. The analytical solution can be found in Ref. [7]. In this unsteady flow case, the directional splitting scheme (DS) is also investigated. First of all, the aforementioned solvers for smooth flow are considered. Then we shall discuss the general BGK solver with a discontinuous distribution function.

3.5.1. Smooth flow solver

The computational domain is chosen as $[0,1]\times[0,1]$ with parameters $U = V = 100$, $\alpha = 0.175$, and $\beta = 0.225$. The boundary values are implemented according to the theoretical solution. The cell size is uniform and the diffusion coefficient is set to be $D = 2$.

The error norms are calculated with different cell size Δx ($=\Delta y$). The computations are all started from the analytical solution at time $t = 4\times10^{-3}$ with time step size fixed to a very small value, $\Delta t = 5\times10^{-10}$, to eliminate errors in time. The error norms L_2 and L_∞ after one time step are presented in Fig. 7(a), which show that the MD scheme, the Q1D extension and the DS method have second-order accuracy in space, and their differences can hardly be seen. According to the aforementioned discussion in Section 2.4, in this linear convection–diffusion case, the omitting of tangential derivatives in a BGK scheme does not affect the spatial accuracy, as there is no viscous stress in the scalar convection–diffusion equation, which is different from the momentum transport.

Similarly the error norms with different computational time step size are calculated with a fine mesh, $\Delta x = 1/1280$. The error norms are computed also after only one time step starting from $t = 2\times10^{-3}$. The error curves in Fig. 7(b) show nonmonotonic behavior. For large value of the CFL number, defined as,

$$\mathrm{CFL} = \frac{\Delta t}{\Delta x}\left(\sqrt{U^2+V^2}+\frac{2D}{\Delta x}\right), \tag{44}$$

all of the schemes are more than second-order accurate in time, which is consistent with the study of Ohwada [34]. Recently, Torrilhon and Xu [35] studied the one-dimensional BGK scheme for the advection–diffusion equation in detail and found this so-called "super-convergence" characteristic. The errors from the MD scheme are more than 50% smaller than those from the Q1D scheme. Thus, the inclusion of tangential slopes of conservative variables in fluxes at the cell interface significantly increases the temporal accuracy.

The same conclusion can be drawn for a high-accuracy gas-kinetic scheme, such as Xu's scheme in low-speed flow [8], where a high-order interpolation of the conservation variables and their slopes at a cell interface

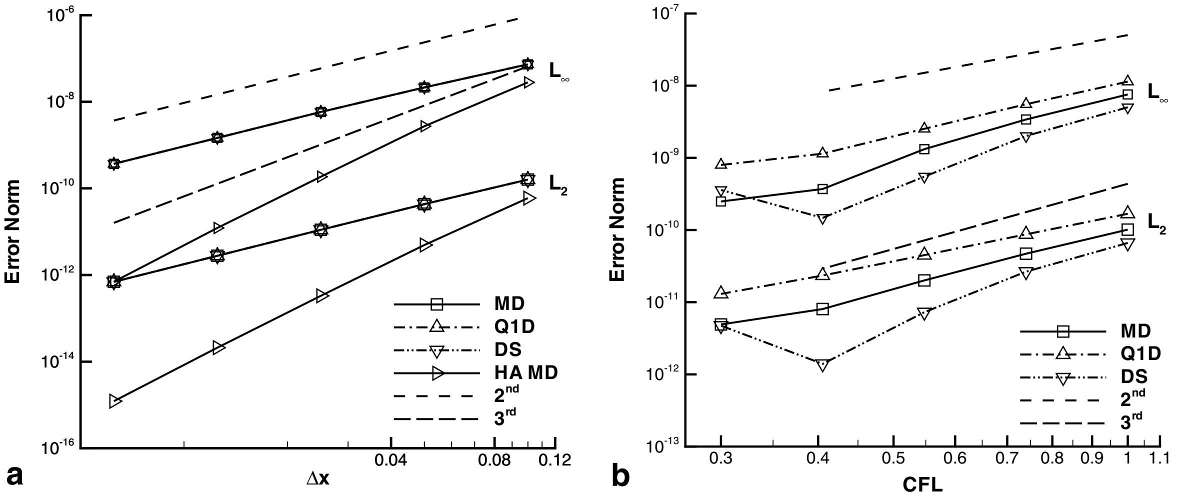

Fig. 7. Variations of error norms with: (a) computational cell size; (b) time step. The lines symbolized by '2nd' and '3rd' indicate the trends of the second-order and third-order accurate schemes, respectively. Both the L_2 and L_∞ norms are normalized by the instantaneous maximal value.

is adopted. Although the accuracy in space is higher than third order, as shown in Fig. 7(a) and represented by 'HA MD', an MD method can yield better results with smaller numerical errors not in space but in time (similar to the present scheme and not presented here).

The DS method can be seen to have clearly smaller errors than the MD one for large CFL number. This can be understood through the conventional (PDE based) directional splitting (operator splitting) method. With the help of intermediate variables $W^{n+1/2}$, the temporal accuracy of a scheme for multidimensional flow may be improved under some conditions.

3.5.2. BGK method with discontinuous distribution function

For the general BGK scheme, the particle distribution function is constructed separately on two sides of a cell interface to capture flow discontinuities, such as shock waves. Here the multidimensional, quasi-one-dimensional extension, and the directional splitting versions are all investigated.

Here we consider the performance of these flow solvers with a fixed CFL number and different grid Reynolds number

$$Re_{\Delta x} = \sqrt{U^2 + V^2}\Delta x/D. \tag{45}$$

That is, the combination of spatial and temporal accuracy is studied. The results is shown in Fig. 8. Again the nonmonotonic behavior can be seen. For a well-resolved flow region, with low grid Reynolds number, the performance differences of the MD, Q1D and DS methods can hardly be seen. With increasing grid Reynolds number, such as $Re_{\Delta x} > 1$, the Q1D shows progressively larger errors, while the DS scheme seems a little better than the MD one. For $Re_{\Delta x} \approx 10$, the Q1D method produces errors almost larger than an order of magnitude. But with a large grid Reynolds number, such as $Re_{\Delta x} > 100$, all the schemes yields similar results. This can be explained as following. As the time step Δt decreases much faster than the cell size Δx for a given CFL number (see Eq. (44)), for low $Re_{\Delta x}$, the effects of Δt becomes much smaller than that of Δx, leading to the small difference of MD, Q1D and DS methods. On the other hand, for large $Re_{\Delta x}$, the flow field is not well resolved, and the artificial dissipation from the discontinuous distribution function in the schemes dominates the errors, resulting in small difference among these methods. The advantage of the MD and DS methods mainly exists in the moderate-$Re_{\Delta x}$ region, corresponding to 'super-convergence' behavior [35].

In Fig. 8 it can be seen that the limiter in the conservative-variables reconstruction of a BGK scheme may spoil the results at very low $Re_{\Delta x}$, when compared to the results from the multidimensional scheme, labeled

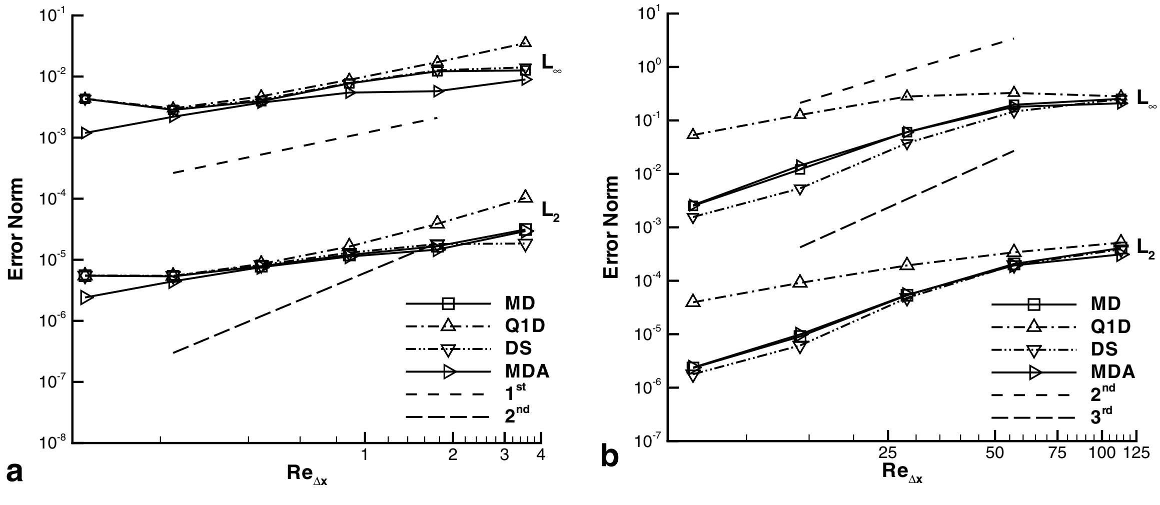

Fig. 8. Variations of error norms with grid Reynolds number. The CFL numbers are all set to be 0.5. The lines symbolized by 'MDA' indicate the results of a multidimensional scheme with central difference to calculate the slopes on both sides of a cell interface. Both the L_2 and L_∞ norms are normalized by the instantaneous maximal value. The calculation is started at time $t_1 = 3 \times 10^{-3}$ and the error is presented at $t_2 = 4.24 \times 10^{-3}$ in (a). The values are $t_1 = 2 \times 10^{-3}$ and $t_2 = 3.75 \times 10^{-3}$ in (b), respectively. In (b) the diffusion coefficient is changed to be $D = 0.0625$ with constants in Eq. (43) $\alpha = 0.175$ and $\beta = 0.375$.

'MDA', with the central difference to calculate the slopes on both sides of a cell interface. But for the large $Re_{\Delta x}$ case, a limiter is necessary to inhibit nonphysical oscillations. The DS scheme also shows good performance. Its low memory requirement and simplicity of written code are also very attractive. In brief, the inclusion of tangential slopes in the MD scheme can clearly increase temporal accuracy.

3.6. Low-Reynolds-number flow around an airfoil

The effect of inclusion of tangential slopes in a BGK method with a discontinuous distribution function is also investigated in the flow around a NACA0012 airfoil. This test case has been previously used as a benchmark for viscous flow [22,36]. The flow conditions are Mach number $M = 0.8$, attack angle $\alpha = 10^0$, Reynolds number $Re = 73$. A C-type mesh with 288×89 cells is adopted. The computational domain is chosen as 10

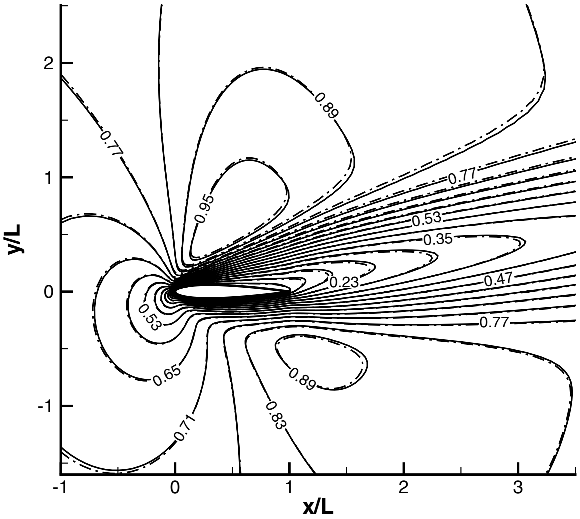

Fig. 9. Mach number contours for NACA0012 airfoil at $M = 0.8$, $\alpha = 10^0$ and $Re = 73$. Solid line is for multidimensional scheme and dash dot quasi-one-dimensional method.

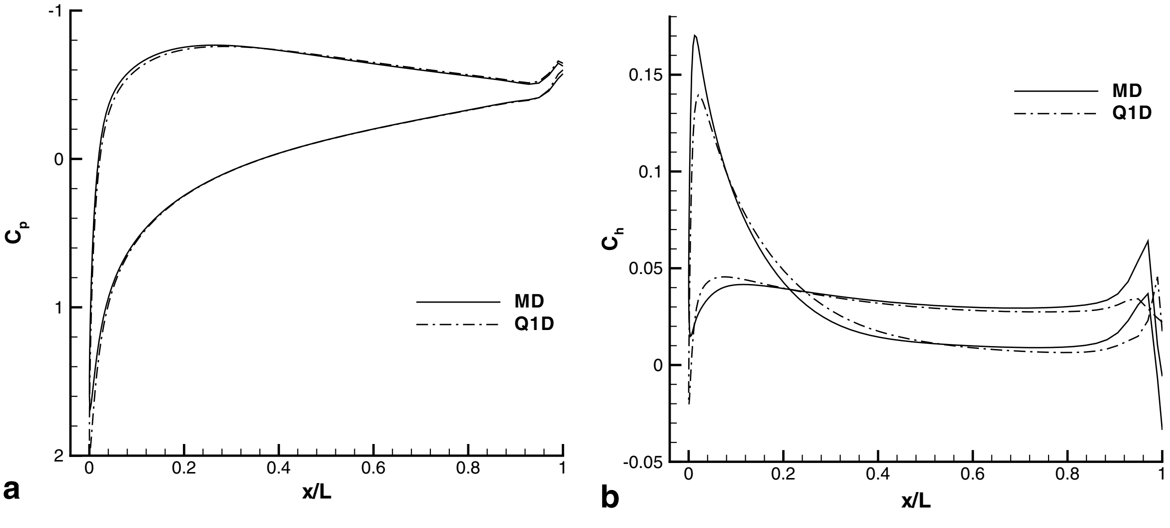

Fig. 10. Pressure coefficient (a) and heat flux coefficient (b) distribution along the NACA0012 airfoil at $M = 0.8$, $\alpha = 10^0$ and $Re = 73$.

times the length of foil chord L, and the normal grid Reynolds number near the surface of the airfoil is about $Re_{\Delta y} = 0.2$. As the flow can be well-resolved, no limiter is used in the reconstruction of variables at a cell interface. Nonreflecting conditions [37] for the far field boundary and isothermal nonslip conditions at the foil surface are used in the present study.

Fig. 9 shows the computed Mach number distributions. The results of the MD and Q1D methods show only a little difference and both agree with those of May et al. [22] calculated with the CUSP scheme. The same conclusion can be drawn for the wall pressure distribution (see Fig. 10(a)) except for the nose region, where the Q1D method yields high pressure. But for some sensitive quantities, such as the wall heat flux, normalized by $\rho_\infty V_\infty^3/2$ and shown in Fig. 10(b), the multidimensional scheme does give obviously different results. However, more numerical and experimental data are required to further validate the computation.

4. Conclusion

The present paper investigates the advantage of the multidimensional gas-kinetic BGK scheme compared with the corresponding quasi-one-dimensional extension and Godunov directional splitting scheme. The construction of an MD BGK scheme with scalar transport in the smooth flow region is introduced with the inclusion of the tangential slopes in the flux computation, which are absent in a Q1D or DS version.

The present study shows that the MD scheme can capture the inverted velocity profile in a rarefied cylindrical Couette flow, the weak flow field induced by a nonuniform wall temperature with low Knudson number, while the Q1D fails. In high-speed microchannel flow and power-law fluid flow between rotating cylinders, the MD scheme can also yield clearly better results than the Q1D method. In the low-Reynolds-number flow around a NACA0012 airfoil case, the MD and Q1D predict wall heat flux distribution with obvious difference. The DS method predicts results nearly identical to those from Q1D in these steady flow cases, except that it is not able to give reasonable solutions in non-Newtonian fluid case with viscous exponential factor away from unity. Correct prediction of the stress and the wall temperature gradient is considered responsible for this better performance.

In the simulation of linear convection–diffusion equation, the present study shows that the inclusion of tangential slopes in the flux is able to increase the accuracy obviously not in space but in time. In this case without viscous stress effect, the directional splitting technique can also improve the temporal accuracy.

However, for some cases, such as computation with a coarse mesh, or with a large grid-Reynolds-number, numerical dissipation may conceal the improvement from the MD scheme. Then a Q1D gas-kinetic BGK scheme or the DS one is a good choice, as an MD scheme takes more computational time, and sometimes a DS method is more robust, and requires less memory. Additionally, for unsteady flow or flow with high-Reynolds number, the performance difference between the MD, Q1D and DS schemes still requires further study. Nevertheless, the present study gives several benchmark test cases for Navier–Stokes solvers, and through them shows that one should be cautious to adopt the Q1D or DS scheme in any case that is sensitive to the accuracy of the stress or wall variable gradient calculation. It is then worthwhile to use the MD scheme for high performance. The present results are also expected to be helpful for the construction and application of other multidimensional methods.

Acknowledgments

This work is supported by the National Natural Science Foundation of China (10302015, 10232020) and China Postdoctoral Science Foundation. The authors would like to thank K. Xu from Hong Kong University of Science and Technology for his helpful comments.

References

[1] R.J. LeVeque, Wave propagation algorithms for multidimensional hyperbolic systems, J. Comput. Phys. 131 (2) (1997) 327–353.

[2] W.A. Wood, W.L. Kleb, Diffusion characteristics of upwind schemes on unstructured triangulations, AIAA Paper 98-2443, 1998.

[3] D. Caraeni, L. Fuchs, Compact third-order multidimensional upwind discretization for steady and unsteady flow simulations, Comput. Fluids 34 (2005) 419–441.

[4] D. Sidilkover, Some approaches towards constructing optimally efficient multigrid solvers for the inviscid flow equations, Comput. Fluids 28 (1999) 551–557.

[5] P. Colella, Multidimensional upwind methods for hyperbolic conservation laws, J. Comput. Phys. 87 (1990) 171–200.

[6] K. Xu, A gas-kinetic BGK scheme for the Navier–Stokes equations, and its connection with artificial dissipation and Godunov method, J. Comput. Phys. 171 (2001) 289–335.

[7] Q.B. Li, S. Fu, K. Xu, A compressible Navier–Stokes flow solver with scalar transport, J. Comput. Phys. 204 (2005) 692–714.

[8] K. Xu, X. He, Lattice Boltzmann method and gas-kinetic BGK scheme in the low-Mach number viscous flow simulations, J. Comput. Phys. 190 (2003) 100–117.

[9] K. Xu, M. Mao, L. Tang, A multidimensional gas-kinetic BGK scheme for hypersonic viscous flow, J. Comput. Phys. 203 (2005) 405–421.

[10] S.K. Godunov, Finite difference methods for numerical computation of discontinuous solutions of the equations of fluid dynamics, Mat. Sbornik 47 (1959) 271–295.

[11] G. Strang, On the construction and comparison of difference schemes, SIAM J. Numer. Anal. 5 (1968) 506–517.

[12] Q.B. Li, S. Fu, Numerical simulation of high-speed planar mixing layer, Comput. Fluids 32 (2003) 1357–1377.

[13] M. Sun, T. Saito, P.A. Jacobs, E.V. Timofeev, K. Ohtani, K. Takayama, Axisymmetric shock wave interaction with a cone: a benchmark test, Shock Waves 14 (5–6) (2005) 313–331.

[14] A. Slyz, K.H. Prendergast, Time-independent gravitational fields in the BGK scheme for hydrodynamics, Astron. Astrophys. Suppl. Ser. 139 (1999) 199–217.

[15] G. May, A. Jameson, Improved gas kinetic multigrid method for three-dimensional computation of viscous flow, AIAA-2005-5106, 17th AIAA Computational Fluid Dynamics Conference, Toronto, Ontario, June 6–9, 2005.

[16] K. Xu, Z. Li, Microchannel flows in slip flow regime: BGK–Burnett solutions, J. Fluid Mech. 513 (2004) 87–110.

[17] T. Ohwada, K. Xu, The kinetic scheme for the full-Burnett equations, J. Comput. Phys. 201 (2004) 315–332.

[18] J. Zhao, Q.B. Li, G. Zhang, S. Fu, Numerical simulation of gas flow in micro-channels with BGK scheme, J. Tsinghua Univ. (Sci. Tech.) 43 (8) (2003) 1083–1087.

[19] Q.B. Li, S. Fu, K. Xu, Application of gas-kinetic scheme with kinetic boundary conditions in hypersonic flow, AIAA J. 43 (10) (2005) 2170–2176.

[20] J.C. Maxwell, On stresses in rarified gases arising from inequalities of temperature, Philos. Trans. Roy. Soc. London 170 (1879) 156–231.

[21] Y. Sone, K. Aoki, S. Takata, H. Sugimoto, A. Bobylev, Inappropriateness of the heat-conduction equation for description of a temperature field of a stationary gas in the continuum limit: Examination by asymptotic analysis and numerical computation of the Boltzmann equation, Phys. Fluids 8 (2) (1996) 628–638.

[22] G. May, B. Srinivasan, A. Jameson, Calculating three-dimensional transonic flowusing a gas-kinetic BGK finite-volume method, AIAA-2005-1397, 43rd AIAA Aerospace Sciences Meeting & Exhibit, Reno, NV, January 10–13, 2005.

[23] S. Yoon, A. Jameson, Lower–upper symmetric Gauss–Seidel method for the Euler and Navier–Stokes equations, AIAA J. 26 (9) (1988) 1025–1026.

[24] K.W. Tibbs, F. Baras, A.L. Garcia, Anomalous flow profile due to the curvature effect on slip length, Phys. Rev. E 56 (2) (1997) 2282–2283.

[25] K. Aoki, H. Yoshida, T. Nakanishi, Inverted velocity profile in the cylindrical Couette flow of a rarefied gas, Phys. Rev. E 68 (2003) 016302.

[26] D.A. Lockerby, J.M. Reese, D.R. Emerson, R.W. Barber, Velocity boundary condition at solid walls in rarefied gas calculations, Phys. Rev. E 70 (2004) 017303.

[27] D. Einzel, P. Panzer, M. Liu, Boundary condition for fluid flow: curved or rough surfaces, Phys. Rev. Lett. 64 (19) (1990) 2269–2272.

[28] Y. Sun, R.W. Barber, D.R. Emerson, Inverted velocity profiles in rarefied cylindrical Couette gas flow and the impact of the accommodation coefficient, Phys. Fluids 17 (2005) 047102.

[29] R.W. Barber, Y. Sun, X.J. Gu, D.R. Emerson, Isothermal slip flow over curved surfaces, Vacuum 76 (2004) 73–81.

[30] E.H. Kennard, Kinetic Theory of Gases, McGraw-Hill, New York, 1938.

[31] Y. Sone, Flow induced by temperature fields in a rarefied gas and their ghost effect on the behavior of a gas in the continuum limit, Annu. Rev. Fluid Mech. 32 (2000) 779–811.

[32] C.K. Oh, E.S. Oran, R.S. Sinkovits, Computations of high speed, high Knudsen number microchannel flows, J. Therm. Phys. Heat Trans. 11 (1997) 497.

[33] R. Raju, S. Roy, Hydrodynamic study of high-speed flow and heat transfer through a microchannel, J. Therm. Heat Trans. 19 (1) (2005) 106–113.

[34] T. Ohwada, On the construction of kinetic schemes, J. Comput. Phys. 177 (1) (2002) 156–175.

[35] M. Torrilhon, K. Xu, Stability and consistency of kinetic upwinding for advection–diffusion equations, IMA J. Numer. Analy. (2006) in press, doi:10.1093/imanum/dr1005.

[36] F. Bassi, S. Rebay, A high-order accurate discontinuous finite element method for the numerical solution of the compressible Navier–Stokes equations, J. Comput. Phys. 131 (1997) 267–279.

[37] T.J. Poinsot, S.K. Lele, Boundary conditions for direct simulations of compressible viscous flows, J. Comput. Phys. 101 (1992) 104–129.